ADVANCED FUNCTIONAL MATERIALS
www.afm-journal.de

Inhibition of Cancer Cell Migration by Gold Nanorods: Molecular Mechanisms and Implications for Cancer Therapy

Teng Zhou, Meifang Yu, Bo Zhang, Liming Wang, Xiaochun Wu, Hejiang Zhou, Yipeng Du, Junfeng Hao, Yaping Tu, Chunying Chen, and Taotao Wei**

Gold nanorods have received much attention because of their distinct physicochemical properties and promising applications in bioimaging, biosensing, drug delivery, photothermal therapy, and optoelectronic devices. However, little is known regarding their effect on tumor metastasis. In the present investigation, serum protein-coated gold nanorods (AuNRs) at low concentrations is shown to exhibit no apparent effects on the viability and proliferation of three different metastatic cancer cell lines, that is, MDA-MB-231 human breast cancer cells, PC3 human prostate cancer cells, and B16F10 mouse melanoma cells, but effectively inhibit their migration and invasion in vitro. Quantitative proteomics and real-time PCR array analyses indicate that exposure of cells to AuNRs can down-regulate the expression of diverse energy generation-related genes, which accounts for their inhibition of mitochondrial oxidative phosphorylation (OXPHOS) and glycolysis. The impairment of OXPHOS and glycolysis results in a distinctive reduction of ATP production and subsequent inhibition of F-actin cytoskeletal assembly, which is crucial for the migration and invasion of cancer cells. The inhibitory effect of AuNRs on cancer cell migration is also confirmed in vivo. Taken together, the unique mechanism in inhibiting cancer cell migration by AuNRs might provide a new approach to specific cancer therapeutic treatment.

1. Introduction

Cancer is a very complicated disease with a variety of hallmarks, and it poses a severe threat to public health.[1,2] The major source of cancer-related deaths is not from the primary tumor itself but from metastasis to other organs in the body.[3] To develop successful metastases, tumor cells need to invade the surrounding host tissue, migrate out of the primary tumor, intravasate into blood or lymphatic vessels, translocate to distant sites, extravasate, adapt to the new local microenvironments, and eventually seed, proliferate and colonize to form secondary tumors.[4–6] Cell migration, a basic event shared by diverse cancer types, is a highly integrated multistep process, and it is generally believed that lamellipodia have a major role in driving cell migration by attaching to a substrate and generating a physical force to pull the cell body forward.[7] Lamellipodia are flat, sheet-like membrane protrusions that form at the leading edges of migrating cells. The driving force for lamellipodia formation is localized polymerization of actin filaments beneath the plasma membrane.[8] Polarized filaments formed by polymerization of actin monomers are referred to as F-actin. These filaments form through the insertion of actin monomers between the plus ends of the filament and the membrane interface, a process mediated by nucleation and elongation factors, which are recruited to the tips of lamellipodia.[9] Assembly of the actin

T. Zhou, M. Yu, Dr. B. Zhang, H. Zhou, Dr. Y. Du, J. Hao, Prof. T. Wei
National Laboratory of Biomacromolecules
Institute of Biophysics
Chinese Academy of Sciences
Beijing 100101, China
E-mail: weitt@moon.ibp.ac.cn

T. Zhou, M. Yu, H. Zhou
University of Chinese Academy of Sciences
Beijing 100049, China

Dr. L. Wang, Prof. X. Wu, Prof. C. Chen
CAS Key Laboratory for Biomedical Effects of Nanomaterials and Nanosafety
National Center for Nanoscience and Technology
Beijing 100190, China
E-mail: chenchy@nanoctr.cn

Dr. L. Wang, Prof. C. Chen
CAS Key Laboratory for Biomedical Effects of Nanomaterials and Nanosafety
Institute of High Energy Physics
Chinese Academy of Sciences
Beijing 100049, China

Prof. Y. Tu
Department of Pharmacology
Creighton University School of Medicine
Omaha, NE 68178, USA

DOI: 10.1002/adfm.201401642

cytoskeleton is an energy-consuming process that can be suppressed in cells by inhibiting ATP generation. This impairment of actin cytoskeletal assembly in turn inhibits the progression of cancer cell migration and invasion.[10]

Conventional anti-cancer drugs display significant weaknesses, which limit their use in cancer therapy.[11] Currently, researchers are pursuing the development of new tools and therapeutic strategies to provide more effective therapies against cancer. Recent advances in nanomedicine, a multidisciplinary field referring to the application of nanomaterials to medicine and healthcare, offer a promising alternative for cancer treatment.[12–14] Due to their small size and facile modification, nanomaterials demonstrate significant advantages in selectively gaining access to cancer cells, either by passive or active targeting. In addition, based on their unique intrinsic characteristics and controlled functional properties, nanomaterials show prospects for broad application in the detection, imaging and therapy of cancer diseases.[15–18]

Among these nanomaterials, gold nanorods (AuNRs) have been widely explored for applications in bioimaging, biosensing, drug delivery and photothermal therapy due to their unique physiochemical and optical properties.[19–24] To date, extensive researches have been performed on the cytotoxicity, biocompatibility and biodistribution of AuNRs with different size, shape and surface modifications.[25–29] Our previous studies have shown that AuNRs exposure causes significant metabolic changes in human alveolar epithelial carcinoma cells and ultimately cell death.[30,31] Similar to other types of gold nanomaterials, AuNRs have a strong ability to bind with –SH or $–NH_2$ containing molecules.[32] Thus, biological molecules, particularly proteins, can serve as important substrates in binding to AuNRs via specific residues. Proteins binding to the surface of nanomaterials form a coating known as the protein corona, which exhibits dynamic characteristics in biological environments and helps reduce potential nanohazards.[33–35] Our recent work has revealed the binding structure of the protein corona on AuNRs, and demonstrated that protein-coated AuNRs have lower cytotoxicity.[36] However, binding of proteins to AuNRs may also alter their biological functions, enabling AuNRs as potential therapeutic agents. Arvizo and co-workers have recently suggested that spherical gold nanoparticles (AuNPs) can serve as self-therapeutic nanoparticles, which inhibit tumor growth and metastasis via reversal of epithelial-mesenchymal transition (EMT) and inhibition of p42/44 MAPK signaling.[37] However, the cellular effects caused by gold nanomaterials and the underlying mechanisms may vary depending on the distinct sizes, shapes and surface coatings of the materials, as well as the cancer cell types being treated. So far, little is known regarding the direct effect of AuNRs on the migration and metastasis of cancer cells.

In the present study, the cytotoxicity of serum protein-coated AuNRs on three different metastatic cancer cell lines was assessed. Moreover, the inhibitory effect of cancer cell migration by AuNRs was evaluated in vitro in these three metastatic cancer cell lines using Transwell assays. In addition, the assembly of the F-actin cytoskeleton, cellular ATP generation, mitochondrial oxidative phosphorylation (OXPHOS) and glycolysis were measured in AuNRs-exposed cancer cells. Futhermore, stable isotope labeling with amino acids in cell culture (SILAC)-based quantitative proteomics combined with real-time PCR array analyses was used to understand the molecular mechanism of the inhibition of cancer cell migration by AuNRs. Finally, the in vivo effect of AuNRs on the migration of MDA-MB-231 cells was also assessed using animal models.

2. Results and Discussion

2.1. Characterization and Cytotoxicity Assessment of AuNRs

AuNRs were prepared according to previously described procedures.[30] To increase their biocompatibilities, as-synthesized AuNRs were washed twice with water, incubated with complete cell culture medium containing 10% fetal bovine serum for 3 h and re-suspended in water to produce serum protein-coated AuNRs. The mean size of the AuNRs was calculated by measuring at least 100 particles using transmission electron microscopy (TEM). The naked AuNRs had an aspect ratio of 4.2 with a mean length of 46.7 ± 5.8 nm and width of 11.1 ± 1.2 nm (**Figure 1**A). The protein-coated AuNRs had a mean length of 54.4 ± 5.2 nm and width of 18.2 ± 1.5 nm (Figure 1B). The longitudinal surface plasmon resonance (SPR) of the naked and the protein-coated AuNRs was approximately 815 and 835 nm (Figure 1C), respectively, as observed by UV–Vis–NIR absorption spectroscopy. The naked AuNRs were positively charged (34.8 ± 1.0 mV) and the protein-coated AuNRs were negatively charged (–29.3 ± 1.9 mV) (Figure 1D), as analyzed using a particle analyzer. These characteristics of AuNRs in current study were consistent with that in our previous reports.[26,30,36] Freshly prepared protein-coated AuNRs were used for all of the studies.

We next investigated the cytotoxicity of AuNRs in three different cancer cell lines. MDA-MB-231 human breast cancer cells, PC3 human prostate cancer cells and B16F10 mouse melanoma cells were exposed to different concentrations of AuNRs for 24 h, and cell viability was determined by both CCK-8 assays and trypan blue-staining assays. After exposure to 50 μM AuNRs for 24 h, more than 90% of cancer cells remained viable as measured by the CCK-8 assays, which is consistent with about 10% increase of dead cells shown in trypan blue-staining assays. These results suggested that low concentrations of AuNRs are not apparently toxic to these cells. However, higher concentrations of AuNRs decreased cell viability in a concentration-dependent manner (Figure 1E–G). Based on these results, a concentration of 50 μM was used in subsequent experiments to investigate the effects of AuNRs on cancer cells.

2.2. AuNRs Attenuate the Migration and Invasion Ability of Cancer Cells

Although gold nanorods might act as functional nanomaterials for diagnosis, drug delivery or photothermal therapy in cancer, little is known about their direct effects on the migration and metastasis of cancer cells. Thus, we performed Transwell assays to investigate these effects. NIH-3T3 fibroblast conditioned medium contains various growth factors and cytokines and is widely employed as a chemoattractant in MDA-MB-231 cell Transwell assays.[38] MDA-MB-231 cells were exposed to 50 μM

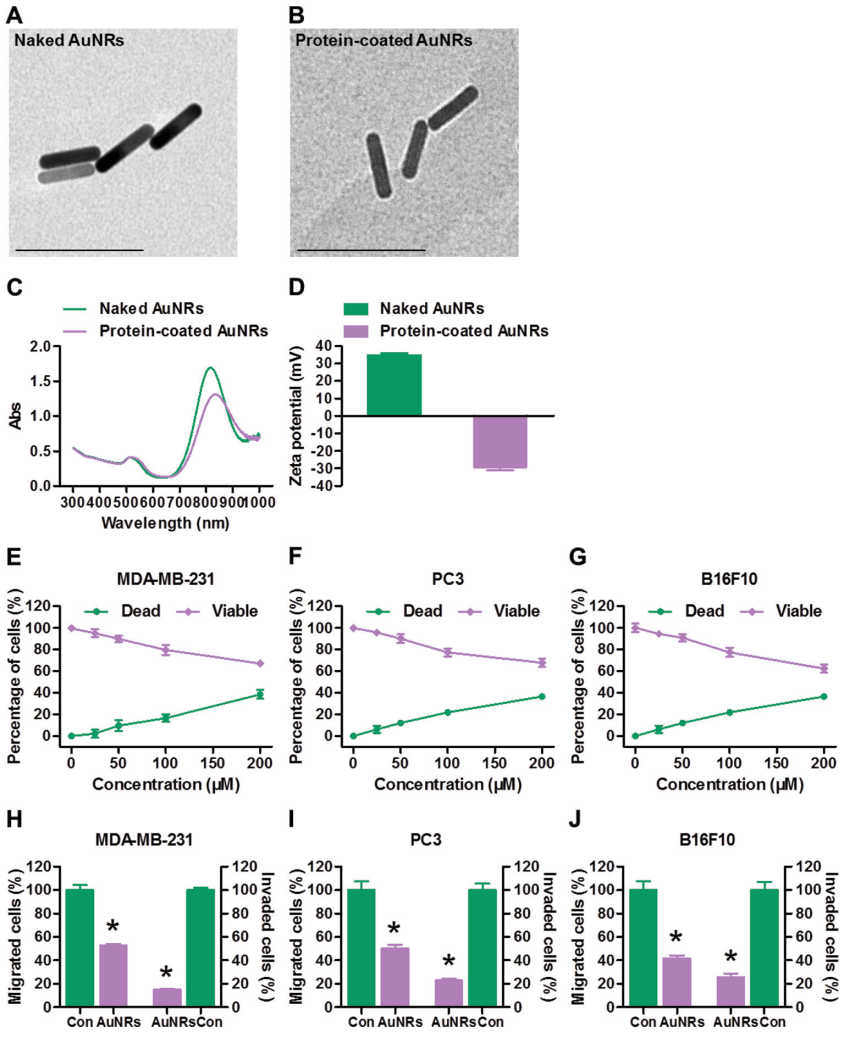

Figure 1. Characterization and cytotoxicity assessment of AuNRs and inhibition of the migration and invasion of metastatic cancer cells by AuNRs. Images of A) naked and B) protein-coated AuNRs were captured using a transmission electron microscope. The scale bar represents 100 nm. C) UV–Vis–NIR absorption spectra of AuNRs. D) Zeta potential of AuNRs. E) MDA-MB-231 cells, F) PC3 cells, and G) B16F10 cells were exposed to AuNRs at different concentrations for 24 h and cytotoxicity of AuNRs was assessed. Percentage of dead cells was determined by trypan blue-staining assays. Percentage of viable cells was determined by CCK-8 assays. Values represent the mean ± SEM, $N = 5$. H) MDA-MB-231 cells, I) PC3 cells, and J) B16F10 cells were preincubated with or without 50 μM AuNRs for 24 h and then subjected to Transwell migration and invasion assays. Cells that migrated and invaded through the membrane were stained, imaged, counted and normalized relative to control. Values represent the mean ± SEM, $N = 3$.

AuNRs for 24 h and then treated with NIH-3T3 cell conditioned medium for 5 h or 17 h to induce migration or invasion, respectively. As shown in Figure 1H, the migration and invasion abilities of MDA-MB-231 cells pretreated with AuNRs were much less than those of control cells. In addition, the effects of AuNRs on the migration and invasion of PC3 cells and B16F10 cells were also studied, with 1% FBS as the chemoattractant. The migration and invasion abilities of PC3 cells (Figure 1I) and B16F10 cells (Figure 1J) were both significantly inhibited after exposure to AuNRs, similar to their effects on MDA-MB-231 cells. Representative images are shown in Figure S1 (Supporting Information). Taken together, these data indicate that exposure to AuNRs can significantly reduce the migration and invasion abilities of diverse metastatic cancer cells.

The proliferation and migration of metastatic cancer cells involve multiple signaling pathways, including MAPK kinase cascades. A recent report suggested that AuNPs could inhibit the growth and metastasis of ovarian cancer cells by inhibiting p42/44 MAPK signaling.[37] In contrast, we found no significant changes in MAPK activation in MDA-MB-231 cells exposed to serum protein-coated AuNRs (Figure S2, Supporting Information), probably due to the different cell types and the different coatings of gold nanomaterials.

2.3. AuNRs Impair the Actin Cytoskeletal Assembly in Cancer Cells

The above data indicate that AuNRs exhibit significant inhibitory effects on the migration and invasion of cancer cells. Next, we further investigated the underlying mechanisms. The migration of cancer cells is a highly orchestrated multistep process. The migrating cell first acquires a characteristic polarized morphology in response to extracellular signals. At the cell front, actin assembly drives the extension of flat membrane protrusions called lamellipodia and of fingerlike protrusions called filopodia. At the leading edge of the lamellipodia, the cell forms adhesions that connect the extracellular matrix to the actin cytoskeleton, which anchors the protrusion and gives traction to the cell body.[10] Cortactin is a monomeric protein located in the cytoplasm of cells, which can be activated by external stimuli to promote the polymerization and rearrangement of the actin cytoskeleton.[39,40] To investigate whether AuNRs exposure changes the actin cytoskeleton of cells, we monitored the morphology of the actin cytoskeleton by staining the cells for F-actin. MDA-MB-231 cells were exposed to 50 μM AuNRs for 24 h and then treated with NIH-3T3 conditioned medium for 5 h to induce migration and invasion. The cells were incubated with Alexa-Fluor 488-labeled phalloidin, cortactin antibody and DAPI and then visualized under a laser scanning confocal microscope. As shown in **Figure 2**A, AuNRs pretreatment partially inhibited the formation of lamellipodia in NIH-3T3 conditioned medium-induced cells, although the cells did develop filopodia in response to these chemotactic cues. AuNRs decreased cell spreading and reduced the extent of lamellipodia in MDA-MB-231 cells by approximately 35%. Furthermore, cortactin activation induced by NIH-3T3 conditioned medium was inhibited as a result of AuNRs pretreatment. In addition, the morphology of the actin cytoskeleton of PC3 cells and B16F10 cells upon AuNRs exposure were also observed.

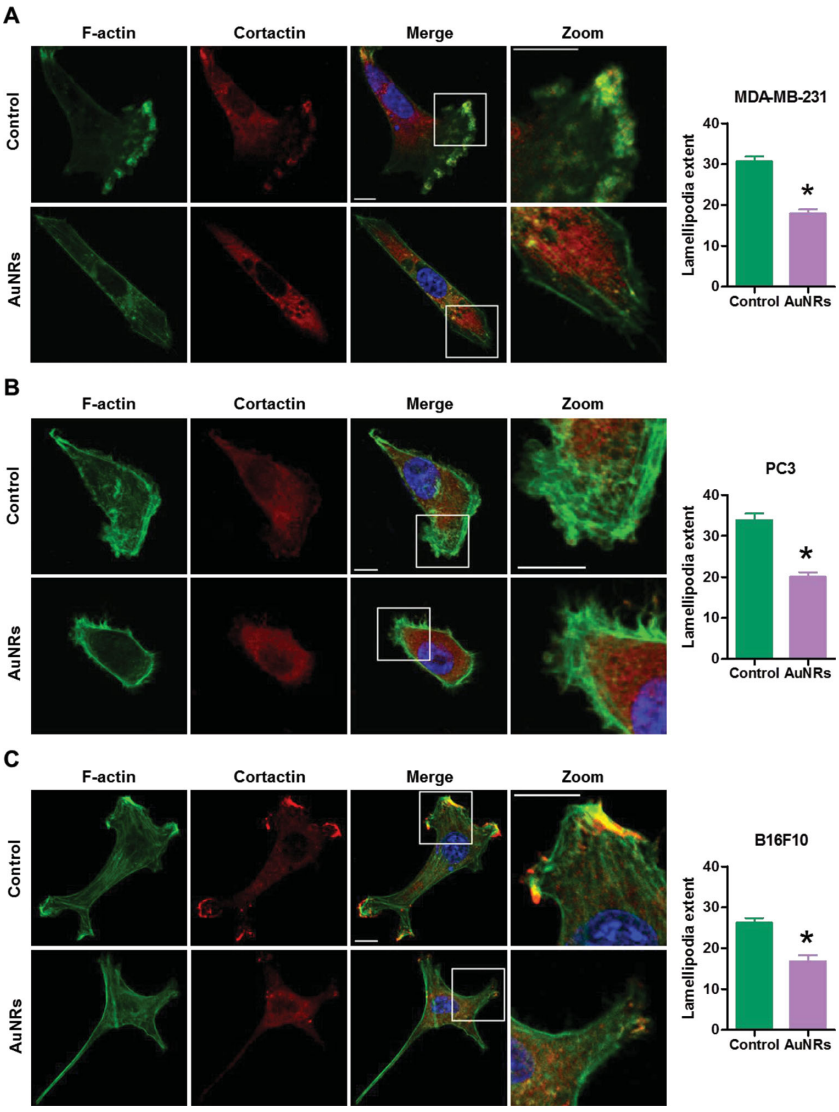

Figure 2. Impairment of F-actin cytoskeletal assembly by AuNRs in cancer cells. A) MDA-MB-231 cells, B) PC3 cells, and C) B16F10 cells were seeded on coverslips, exposed to 50 μM AuNRs for 24 h, treated with NIH-3T3 conditioned medium for 5 h, and then stained with Alexa-Fluor 488-labeled phalloidin for F-actin (green), an antibody against cortactin (red) and DAPI for nuclei (blue). Lamellipodia extents at the cell edges were quantified as a percentage of the cell circumference in 30 randomly selected cells in each group. Scale bar, 10 μm. Values represent the mean ± SEM.

Similarly, the cell spreading and the extent of lamellipodia formation in PC3 cells (Figure 2B) and B16F10 cells (Figure 2C) were also significantly reduced after exposure to AuNRs. These results show that AuNRs reduce the ability of three different cancer cells to migrate and invade, mainly by inhibiting the assembly of the F-actin cytoskeleton.

2.4. AuNRs Decrease the Mitochondria Membrane Potential and ATP Synthesis

Since F-actin cytoskeletal assembly is a process that consumes ATP in cells,[41] we further studied whether AuNRs exposure attenuated F-actin cytoskeletal assembly via the suppression of ATP synthesis. We measured the cellular ATP level of AuNRs-exposed MDA-MB-231 cells using luciferase-based luminescence assays. MDA-MB-231 cells were exposed to 50 μM AuNRs for 24 h and the cellular ATP level was quantified. In comparison with the control MDA-MB-231 cells, AuNRs-treated cells exhibited ATP levels that were decreased by approximately 40%, as shown in **Figure 3**A. In mammalian cells, mitochondria are the centers for cellular energy generation. Thus, we investigated the effect of AuNRs on mitochondrial membrane potential (MMP) using tetramethylrhodamine methylester (TMRM). TMRM is a cell-permeable positively charged dye that readily accumulates in active mitochondria due to their relative negative charge. Thus, depolarized mitochondria with decreased MMP fail to sequester TMRM. The fluorescence intensity of TMRM is directly related to the status of MMP. MDA-MB-231 cells were exposed to 50 μM AuNRs for 24 h, incubated with TMRM for 20 min, harvested by trypsinization, washed with PBS and then fluorescence was quantified by flow cytometry. As shown in Figure 3B, a significant decrease in MMP was observed in MDA-MB-231 cells exposed to AuNRs. Taken together, these data indicated that AuNRs exposure significantly decreases both MMP and ATP synthesis in cancer cells.

2.5. AuNRs Decrease Mitochondrial Oxidative Phosphorylation and Glycolysis

Cellular ATP and energy status is largely generated by mitochondrial oxidative phosphorylation (OXPHOS) and glycolysis. We measured the oxygen consumption rate (OCR), which is indicative of OXPHOS, by using a Seahorse XF24 Extracellular Flux Analyzer under various conditions and treatments (Figure 3C). We calculated the basal respiration by measuring the initial oxygen consumption and subtracting the residual oxygen consumption in the presence of the electron transport complex I and III inhibitors, antimycin A and rotenone, respectively. The decreased oxygen consumption observed upon the addition of oligomycin, which blocks ATP synthase, indicates coupled respiration. Maximal respiration can be calculated by the addition of carbonyl cyanide p-trifluoromethoxyphenylhydrazone (FCCP), a potent mobile protonophore, which uncouples mitochondrial ATP generation from oxygen consumption by transporting protons across the mitochondrial inner membrane instead of through the proton channel of ATP synthase. Upon the addition of FCCP, the increased respiratory capacity above the basal respiration

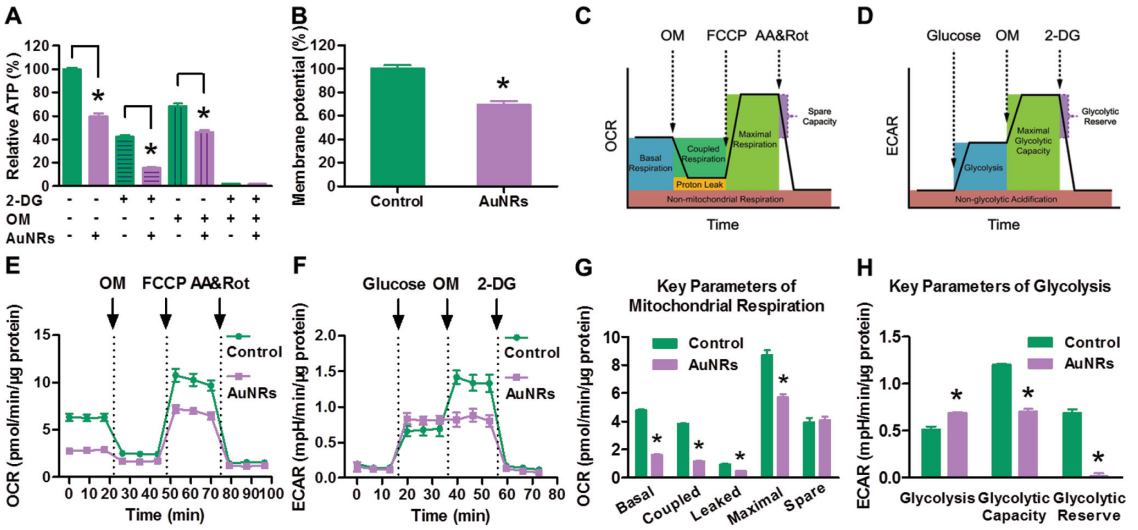

Figure 3. Reduced ATP synthesis via decrease in the mitochondrial oxidative phosphorylation and glycolysis by AuNRs in MDA-MB-231 cells. A) MDA-MB-231 cells were incubated with or without 100 mM 2-deoxyglucose (2-DG), 1 μM oligomycin (OM) or 50 μM AuNRs for 24 h, as indicated. The intracellular ATP level was measured using a luciferase-based luminescence assay and was normalized to protein concentrations. Values represent the mean ± SEM, $N = 3$. B) MDA-MB-231 cells were incubated with or without 50 μM AuNRs for 24 h and then stained with TMRM. Fluorescence intensity of TMRM is proportional to the level of mitochondrial membrane potential. The fluorescence intensity of the mitochondrial membrane potential was analyzed using flow cytometry. Values represent the mean ± SEM, $N = 3$. C) Schematic diagram of the calculation basis of some key parameters in OCR analysis. D) Schematic diagram of the calculation basis of some key parameters in ECAR analysis. E) MDA-MB-231 cells were seeded in specialized 24-well plates and incubated with or without 50 μM AuNRs for 24 h. OCR was monitored using the Seahorse XF24 Extracellular Flux Analyzer in real time. Values represent the mean ± SEM, $N = 5$. F) MDA-MB-231 cells were seeded in specialized 24-well plates and incubated with or without 50 μM AuNRs for 24 h. ECAR was monitored using the Seahorse XF24 Extracellular Flux Analyzer in real time. Values represent the mean ± SEM, $N = 5$. G) Key parameters of mitochondrial respiration tested in (C) as calculated according to (E). H) Key parameters of glycolysis tested in (D) as calculated according to (F). OM, oligomycin. FCCP, carbonyl cyanide p-trifluoromethoxyphenylhydrazone. 2-DG, 2-deoxyglucose. AA, antimycin A. Rot, rotenone.

provides the spare respiratory capacity. As shown in Figure 3E, treatment of MDA-MB-231 cells with AuNRs for 24 h showed significantly reduced OCR compared with controls. Analysis of the key parameters of mitochondrial respiration indicated a large decrease in basal and coupled respiration, as well as a significant decrease in maximal respiration (Figure 3G).

We also measured the extracellular acidification rate (ECAR), which is indicative of glycolysis, by using a Seahorse XF24 Extracellular Flux Analyzer (Figure 3D). Upon addition of a saturating concentration of glucose (10 mM), glucose is taken up by the cells and catabolized via the glycolytic pathway into lactate, resulting in a rapid increase in ECAR. This glucose-induced response is a reflection of basal glycolysis. However, upon the addition of oligomycin, the subsequent increase in ECAR reveals the maximal glycolytic capacity. The difference between the maximal glycolytic capacity and the level of basal glycolysis defines the glycolytic reserve. When cells suffer from an impairment of mitochondrial OXPHOS function, they tend to enhance their glycolytic activities to offset the reduction in energy generation. This was observed in AuNRs-treated MDA-MB-231 cells. Upon the addition of glucose, ECAR increased to even higher level in AuNRs-treated cells compared to control cells (Figure 3F). However, the maximal glycolytic capacity was markedly decreased by AuNRs treatment, as shown by the significant decrease in ECAR compared to the control upon the addition of oligomycin. Overall, cells treated with AuNRs show a marked decrease in maximal glycolytic capacity and a slight increase in basal glycolysis, with an abrogation of glycolytic reserve (Figure 3F,H).

To further confirm the effects of AuNRs on mitochondrial OXPHOS and glycolysis, AuNRs-exposed MDA-MB-231 cells were treated with oligomycin (for inhibition of mitochondrial OXPHOS) or 2-deoxyglucose (2-DG, for inhibition of glycolysis) and cellular ATP level was quantified by luciferase-based luminescence assays. When mitochondrial OXPHOS was inhibited by oligomycin, cellular ATP was decreased to approximately 69% of control cells, and AuNRs exposure further decreased the ATP to approximately 46% of control cells (Figure 3A). Moreover, when glycolysis was inhibited by 2-DG, cellular ATP was decreased to approximately 42% of control cells, and AuNRs exposure further decreased ATP to approximately 16% of control cells (Figure 3A). These findings were consistent with data from the Seahorse assays.

In addition, the OCR and ECAR of PC3 cells and B16F10 cells upon AuNRs treatment were also measured using a Seahorse XF24 Extracellular Flux Analyzer. Similar to results in MDA-MB-231 cells, the mitochondrial respiration and glycolysis in PC3 cells (Figure S3A, S3B, S3C and S3D) and B16F10 cells (Figure S3E–H, Supporting Information) significantly decreased after exposure to AuNRs. Therefore, after AuNRs treatment, cancer cells undergo cellular energy reprogramming and lose their ability to compensate the energy deficiency despite the slight increase in basal glycolysis, due to large decreases both in mitochondrial OXPHOS and in maximal glycolytic capacity.

2.6. AuNRs Localize to Lysosomes and the Cytoplasm in MDA-MB-231 Cells

The cellular effects of AuNRs documented above presumably require their uptake and specific localization in cells. Cellular uptake and trafficking are complex processes comprised of mutiple types and pathways.[42,43] Zhang and coworkers reported that PDDAC-capped AuNRs can be taken up by MDA-MB-231 cells via clathrin-mediated endocytosis, distributed into lysosomes and the cytoplasm, and retained in cells due to re-endocytosis.[28] We quantitatively assessed the cellular uptake of AuNRs using inductively coupled plasma mass spectrometry (ICP-MS). The uptake of AuNRs by MDA-MB-231 cells was time-dependent, with a faster rate at the initial stage that gradually slowed to reach equilibrium (Figure S4, Supporting Information). TEM provides a powerful tool to localize AuNRs in cells with high resolution. We assessed the intracellular trafficking and localization of AuNRs in MDA-MB-231 cells with TEM. Consistent with other reports,[28,30,44,45] AuNRs were internalized and mainly trafficked to endosomes and lysosomes within the first 3 h (**Figure 4**A,B). With incubation for 6 h, more AuNRs entered the cell and a few were seen to escape from the lysosome into the cytoplasm (Figure 4D,E). Escaped AuNRs in the cytoplasm were then recycled via cytoprotective autophagy and finally reached a state of equilibrium, as seen at 24 h (Figure 4G,H). Autophagy is constitutively present in cells to maintain the homeostasis of the cells.[46] However, western blot analyses of the autophagy proteins LC3 and p62 indicated that AuNRs did not change the autophagy level of the cells under our conditions (Figure S5B, Supporting Information). In addition, the mitochondria gradually became swollen and rounded, with irregular and partially disappeared crista (Figure 4C,F,H,I). Further, representative images obtained by super-resolutional three-dimensional structured illumination microscopy (3D-SIM) showed that mitochondria primarily formed tubular network structures in control cells but became dot-like structures and lost their tubular networks in AuNRs-treated cells (Figure S6, Supporting Information). These findings are consistent with the previously described mitochondrial functional alterations, and it is supposed to be an effect of the escaped AuNRs. The intracellular colocalization of AuNRs with specific organelles further support this conclusion. The location of AuNRs can be imaged using two-photon fluorescence confocal microscopy. In these experiments, Mito Tracker Red and Lyso Tracker Red are specific probes that emit red fluorescence for intracellular mitochondria and lysosomes, respectively. The combination of green (AuNRs) and red (organelle probes) signals indicates the intracellular location of the AuNRs. Results from these analyses indicated that AuNRs largely colocalize with lysosomes at 6 h, but that a portion of the AuNRs escape into the cytoplasm at 24 h (Figure S7, Supporting Information).

2.7. AuNRs Down-Regulate the Expression of Energy Generation-Related Proteins in MDA-MB-231 Cells

Next, we asked whether AuNRs affect the expression of energy generation-related proteins. Quantitative proteomic analysis using stable isotope labeling with amino acids in cell culture (SILAC) coupled with 2D-LC-MS/MS was employed to identify and quantify the proteomic changes that occur in AuNRs-treated MDA-MB-231 cells, as summarized in **Figure 5**A. Overall, 1852 cellular proteins were identified and quantified. With a 1.2-fold cutoff, 96 proteins were up-regulated and 343 proteins were down-regulated in AuNRs-treated MDA-MB-231 cells (Figure 5B). The remaining proteins were considered as non-significant changes. To validate the validity of the results, three proteins with typically different SILAC quantitative ratios (GAPDH, β-tubulin and LRP1) and for which antibodies were available were chosen to be re-quantified using western blot analyses. As presented in Figure 5C, the western blot results showed that the ratios of these proteins between AuNRs-treated and control cells were similar to those obtained with SILAC. Gene Ontology (GO) analysis, the key functional classification of NCBI,

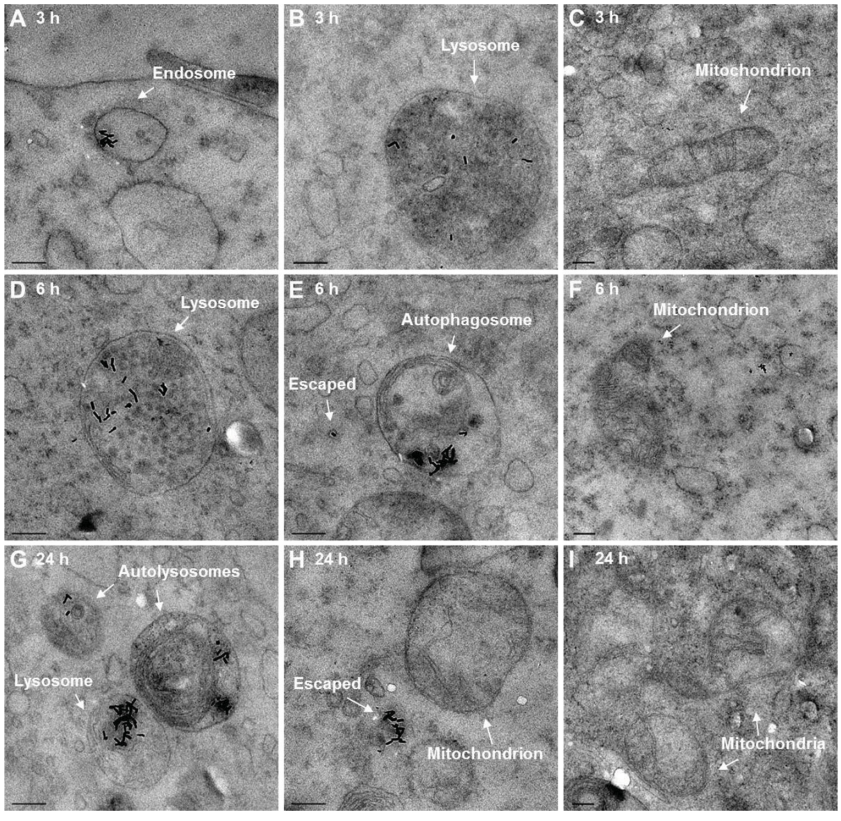

Figure 4. Intracellular localization of AuNRs observed by TEM. MDA-MB-231 cells were incubated with 50 μM AuNRs for A–C) 3 h, D–F) 6 h, or G–I) 24 h, and TEM images were obtained following protocols described in the Experimental Section. Scale bar, 200 nm.

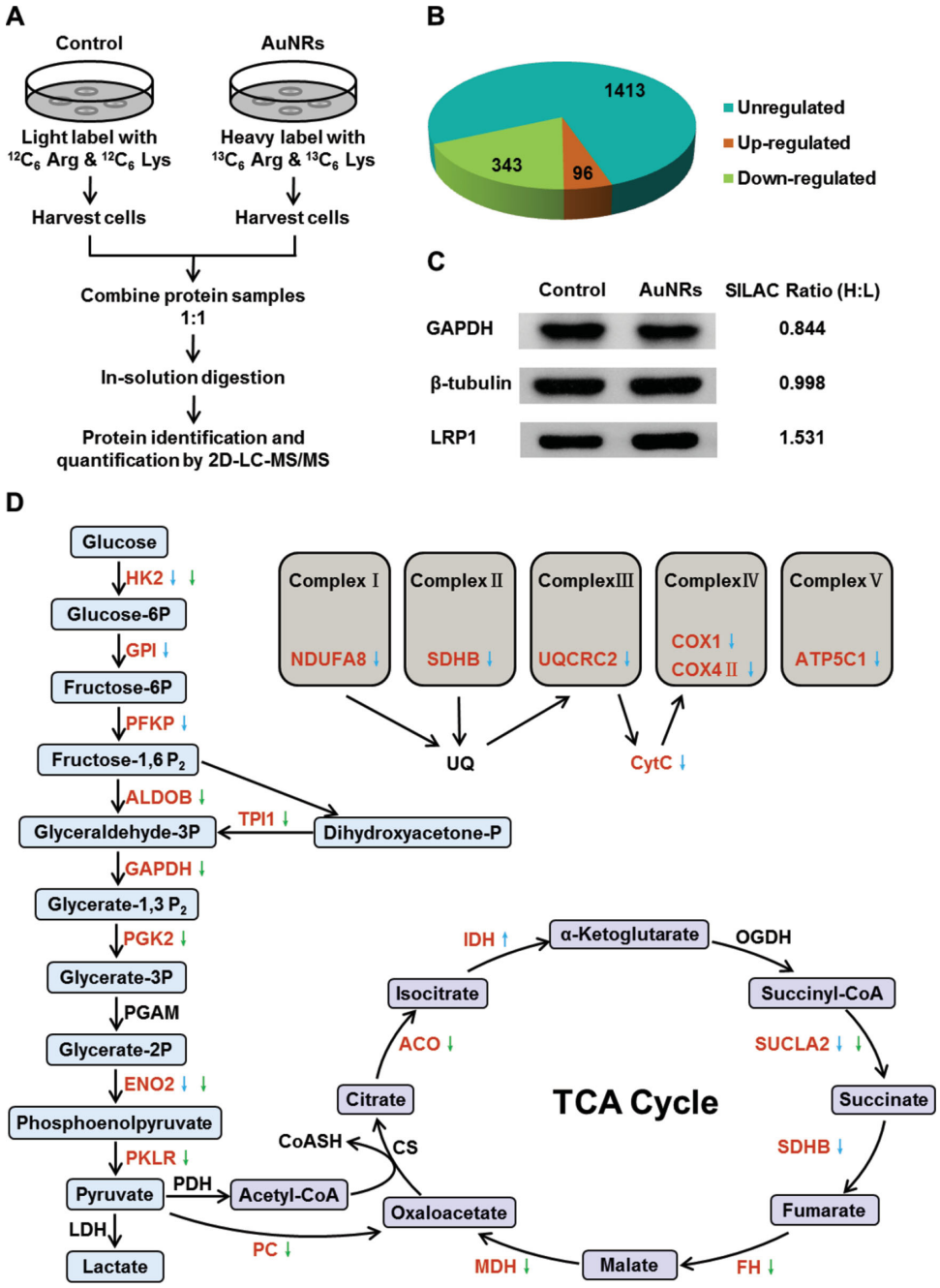

Figure 5. Down-regulation of the expression of energy generation-related proteins by AuNRs in MDA-MB-231 cells analyzed via SILAC-based proteomics and real-time PCR arrays. A) Schematic representation of SILAC strategy coupled with 2D-LC-MS/MS. MDA-MB-231 cells were incubated with (heavy label) or without (light label) 50 μM AuNRs for 24 h and followed by subsequent analyses. B) Pie chart displaying the overall protein expression regulation of MDA-MB-231 cells upon AuNRs treatment with a 1.2-fold cutoff. C) Representative protein quantitative confirmation using western blot analyses. D) Schematic of the glycolysis pathway, TCA cycle pathway and mitochondrial electron trasfer complexes-related protein expression in MDA-MB-231 cells treated with AuNRs. Blue arrows indicate the protein expression regulations analyzed using SILAC-based proteomics, and the green arrows indicate regulations analyzed using real-time PCR arrays.

was performed to identify the main functions of the differentially expressed proteins.[47,48] These results showed that the most affected biological function of MDA-MB-231 cells upon AuNRs treatment was the small molecule metabolic process (Figure S8, Supporting Information). In addition, Path-Net analysis was performed to analyze the interaction among the significant pathways of differentially expressed proteins, based on the Path-Net, which was built according to the interaction among pathways of the Kyoto Encyclopedia of Genes and Genomes (KEGG) database.[49] As presented in Figure S9 (Supporting Information), the key energy metabolism-related pathways, particularly the glycolysis/

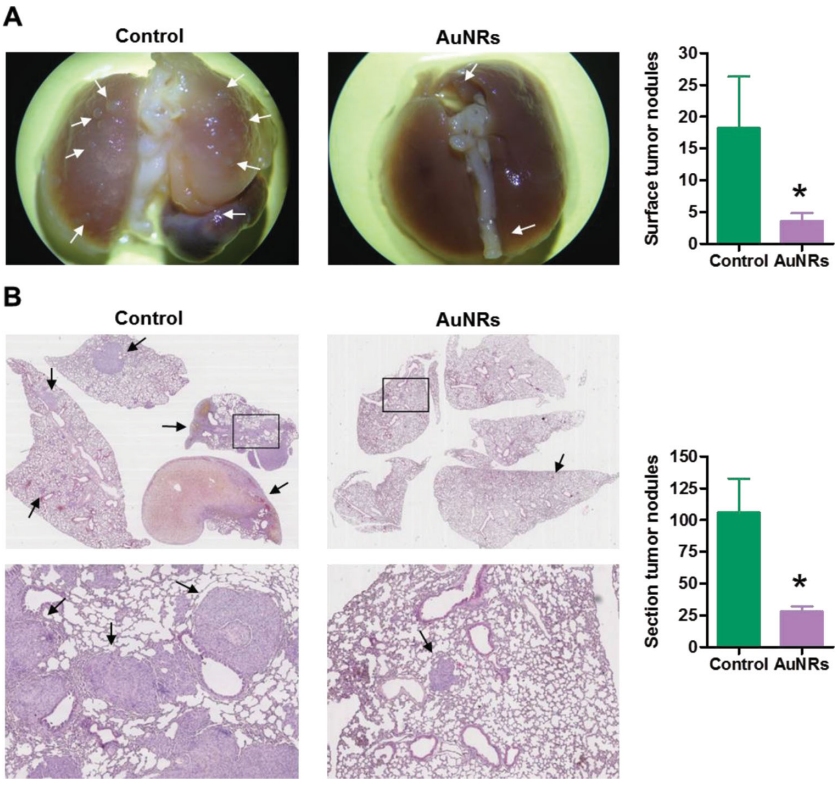

Figure 6. Inhibition of the metastatic ability of MDA-MB-231 cells in vivo by AuNRs. A) MDA-MB-231 control cells or AuNRs-pretreated (50 μM for 24 h) cells were injected into the tail vein of nude mice. After 12 weeks, lungs were isolated and metastatic nodules in lung surface were macroscopically quantified. The white arrows indicate the surface tumor nodules. Values represent the mean ± SEM, $N = 5$. Mann-Whitney test. B) The lungs isolated from (A) were further paraffin-embedded, sectioned and stained with hematoxylin and eosin (H&E). Nodules rich in densely packed cells, as indicated by the black arrows, were quantified as tumor nodules. The rectangular areas in the upper panels are further magnified at the bottom. Values represent the mean ± SEM, $N = 5$. Mann-Whitney test.

gluconeogenesis and TCA cycle pathways, showed a significant response to AuNRs treatment.

To further examine the energy generation-related counterparts of the differentially expressed proteins, specifically glycolysis and OXPHOS, we performed real-time PCR assays using the RT^2 Profiler Human Glucose Metabolism PCR Arrays to quantify mRNA of genes involved in glucose metabolism. As shown in Figure 5D, both SILAC-based proteomics and real-time PCR array analyses indicated that AuNRs treatment down-regulated the expression of multiple proteins involved in glycolysis pathway, TCA cycle pathway and mitochondrial electron transfer complexes. Extensive down-regulation of these proteins is responsible for the impairment of mitochondrial oxidative phosphorylation and glycolysis, which in turn contribute to the decreased ATP generation in AuNRs-treated cells. Taken together, quantitative proteomics and real-time PCR array analyses suggest that the expression of energy generation-related proteins is down-regulated by AuNRs treatment, resulting in impairment of mitochondrial oxidative phosphorylation and glycolysis and decreased ATP generation in MDA-MB-231 cells.

2.8. AuNRs Decrease the Metastatic Ability of MDA-MB-231 Cells in Nude Mice

As mentioned above, AuNRs exposure attenuated the migration and invasion abilities of mutiple metastatic cancer cells in vitro, owing to its inhibitory effect on energy generation and cell motility. To determine AuNRs' effects in vivo, MDA-MB-231 human breast cancer cells treated with AuNRs were examined in mouse models. MDA-MB-231 cells were treated with 50 μM AuNRs for 24 h, which did not show an apparent decrease in cell viability, as shown in Figure 1D. In addition, we found that proteins involved in classical apoptosis (caspase 3 and PARP) and autophagy (LC3 and p62) were not activated upon 50 μM AuNRs treatment in MDA-MB-231 cells (Figure S5, Supporting Information), eliminating concerns about apoptosis or autophagy. We examined the tumorigenicity and proliferative ability of AuNRs-pretreated MDA-MB-231 cells subcutaneously injected into appropriate host Balb/c nude mice following xenograft assays. Subcutaneous implantation of AuNRs-pretreated MDA-MB-231 cells efficiently induced tumors with comparable sizes to those of control cells (Figure S10, Supporting Information), suggesting unchanged characteristics of tumorigenicity and proliferation. We next investigated the metastatic ability of AuNRs-pretreated MDA-MB-231 cells that were intravenously injected into the mouse tail vein. A specific number of surface metastatic nodules were observed in animals injected with MDA-MB-231 control cells, whereas few tumors were detectable in animals injected with AuNRs-pretreated cells (**Figure 6**A). In addition, lungs were paraffin-embedded, sectioned, stained with hematoxylin and eosin, panoramically scanned with a Leica SCN 400 scanner, and metastatic nodules quantified. Consistent with the observations for surface metastatic nodules, there was a significant reduction in metastatic nodules in lung sections of mice injected with AuNRs-pretreated cells compared to untreated cells (Figure 6B). These results indicate that AuNRs-pretreated MDA-MB-231 cells do not manifest changes of tumorigenicity and tumor growth but have significantly decreased lung metastasis activity.

3. Conclusion

In this study, we show that serum protein-coated AuNRs at low concentrations exhibited no apparent effects on the viability and proliferation of three different metastatic cancer cell lines, that is, MDA-MB-231 cells, PC3 cells and B16F10 cells, but effectively inhibited their migration and invasion in vitro.

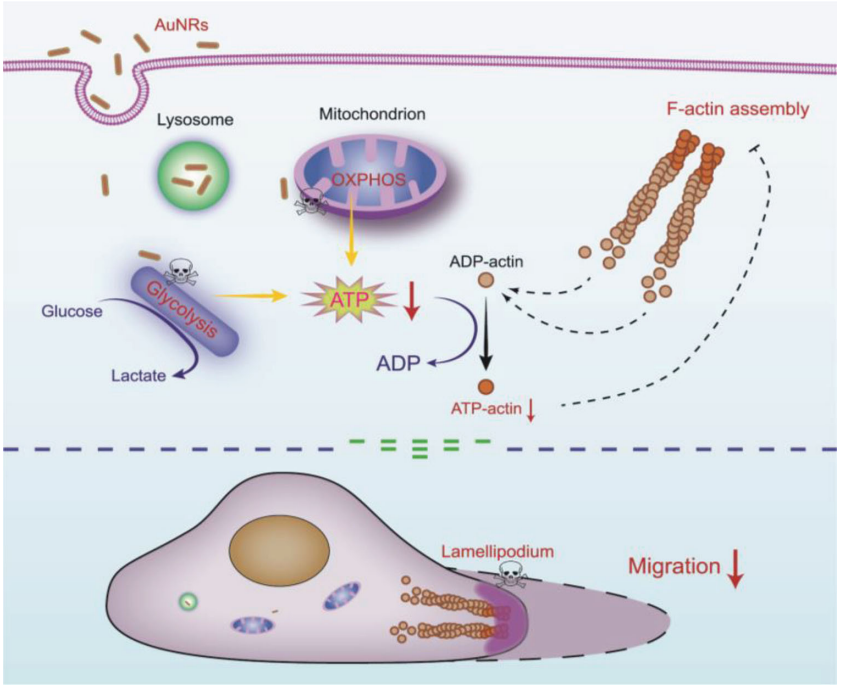

Figure 7. Schematic illustration of the effect of AuNRs on the migration of cancer cells via an impairment in energy production.

Moreover, further mechanism investigations indicate that when AuNRs were endocytosed by cancer cells, they down-regulated the expression of energy generation-related proteins, decreased mitochondrial oxidative phosphorylation and glycolysis, and reduced ATP synthesis. Insufficiency of ATP energy then caused a decrease in F-actin cytoskeletal assembly, which was responsible for the impaired cancer cell migration (**Figure 7**). The inhibitory effect of AuNRs on the metastatic ability of MDA-MB-231 cells was also confirmed in vivo by animal experiments. These findings provide comprehensive insights into the inhibitory effects and underlying mechanisms of AuNRs on metastatic cancer cells and provide a new direction for future investigations of AuNRs as anti-metastatic agents.

4. Experimental Section

Materials: Sodium borohydride ($NaBH_4$), hydrogen tetrachloroaurate (III) trihydrate ($HAuCl_4.3H_2O$), cetyltrimethyl-ammonium bromide (CTAB), silver nitrate ($AgNO_3$), sodium sulfate (Na_2SO_4) and L-ascorbic acid (AA) were purchased from Alfa Chemicals (Bracknell, UK). Cell culture medium and fetal bovine serum (FBS) were purchased from Hyclone (Logan, UT, USA). Cell culture petri dishes were purchased from BD Biosciences (San Jose, CA, USA). Cell Counting Kit (CCK-8) was purchased from Dojindo Laboratories (Kumanoto, Japan). Tetramethylrhodamine methyl ester (TMRM), Mito Tracker Red, Lyso Tracker Red and Alexa-Fluor 488-labeled phalloidin were purchased from Life Technologies (Grand Island, NY, USA). Antibodies for cortactin, caspase 3, PARP, SQSTM1/p62, total and phospho-p44/42 MAPK, total and phospho-SAPK/JNK, total and phospho-p38, Actin, Tubulin, GAPDH, were purchased from Cell Signaling Technology (Danvers, MA, USA). Antibodies for LC3 were purchased from Medical and Biological Laboratories (Nagoya, Japan). Antibodies for LRP1 were purchased from Abcam (Cambridge, UK). The XF Cell Mito Stress Test Kit and XF Glycolysis Stress Test Kit were obtained from Seahorse Bioscience (North Billerica, MA, USA). SILAC Protein Quantitation Kit, $^{13}C_6$L-lysine-2HCl and $^{13}C_6$L-arginine-HCl were obtained from Pierce (Rockford, IL, USA). Other reagents were manufactured in China and were of analytical grade.

Preparation and Characterization of AuNRs: The seed-mediated growth method was employed to synthesize CTAB-capped AuNRs, as described in previous studies.[30] Briefly, 7.5 mL 0.1 M CTAB were mixed with 250 μL 10 mM $HAuCl_4$ and the volume was adjusted to 9.4 ml by adding distilled water. Then, a 0.6 mL ice-cold $NaBH_4$ aqueous solution (0.01 M) was added to the above mixture. CTAB-capped Au seeds formed immediately and were used within 2–5 h. The growth solution for AuNRs consisted of a mixture of 100 mL 0.1 M CTAB, 5 mL 0.01 M $HAuCl_4$, 1 mL 10 mM $AgNO_3$, 2 mL 0.5 M H_2SO_4, and 800 μL 0.1 M Ascorbic acid. Growth was initiated by adding 240 μL of seeds and stopped after 12 h by centrifuging twice at 12 000 ×*g* for 10 min. The as-synthesized AuNRs were further washed another two times, incubated with complete medium containing 10% fetal bovine serum for 3 h and re-suspended in water to produce protein-coated AuNRs. The size and shape of the AuNRs was characterized using transmission electron microscopy (TEM, Tecnai Spirit). The UV–Vis–NIR absorption spectrum of AuNRs was obtained using a Hitachi U-3900 spectrophotometer. The surface charge (zeta-potential) of AuNRs was analyzed using a Beckman Coulter Delsa Nano C particle analyzer according to protocols provided by the manufacturer.

Cell Culture: MDA-MB-231 human breast cancer cells, PC3 human prostate cancer cells, B16F10 mouse melanoma cells and NIH-3T3 mouse embryonic fibroblast cells were obtained from American Type Culture Collection (ATCC; Manassas, VA, USA) and were cultured under conditions recommended by ATCC. For stable isotope labeling, medium deficient in lysine and arginine from the SILAC Protein Quantitation Kit was divided into two fractions, one supplemented with $^{12}C_6$L-lysine-2HCl and $^{12}C_6$L-arginine-HCl, and the other with $^{13}C_6$L-lysine-2HCl, and $^{13}C_6$L-arginine-HCl, to produce light or heavy SILAC medium, respectively. Next, newly subcultured MDA-MB-231 cells were grown in parallel in both media. After at least seven population doublings, the cells had achieved nearly complete incorporation of heavy L-lysine and heavy L-arginine.

Cell Viability Assays: The viabilities of the MDA-MB-231 cells, PC3 cells and B16F10 cells were assessed by both trypan blue-staining assays and CCK-8 assays. For trypan blue-staining assays, cells were seeded in 60 mm cell culture petri dishes and then exposed to different concentrations of AuNRs (0, 25, 50, 100, and 200 μM, respectively) at 37°C for 24 h. Cells were stained with trypan blue, with dead cells colored blue and live cells with intact cell membranes not colored. The number of dead and viable cells was quantified using an automated cell counter IC1000 (Inno-Alliance, Seattle, WA, USA). For CCK-8 assays, cells were seended in 96 well microplates and exposed to different concentrations of AuNRs (0, 25, 50, 100, and 200 μM, respectively) at 37 °C for 24 h. Then CCK-8 was added to each well and incubated for another 2 h. The absorbance of solution was recorded at 450 nm with a Thermo microplate reader.

Transwell Migration and Invasion Assays: Matrigel invasion assays were performed at 37 °C using 24-well Transwell inserts (Corning) coated with 30 μg of Matrigel (BD Biosciences).[38,50] After incubation with or without 50 μM AuNRs for 24 h, cancer cells (50 000) suspended in 200 μL of serum-free medium were seeded into the upper chamber. Next, 600 μL of the migration inducer was placed in the lower chamber. The invasion

of MDA-MB-231 cells was induced by NIH-3T3 cell conditioned medium, and the invasion of PC3 cells and B16F10 cells was induced by 1% FBS. Transwell cell migration assays were performed similarly without Matrigel. Cells that migrated and invaded through the membrane were quantified, and the data were normalized to those of the control cells.

Observation of Actin Cytoskeletal Assembly: The actin cytoskeletal assembly was stained with phalloidin. Briefly, cells were cultured on coverslips, incubated with or without 50 μM AuNRs for 24 h, treated with NIH-3T3 conditioned medium for 5 h, and then fixed with 4% paraformaldehyde in PBS. Cells were permeabilized with 0.1% Triton X-100 and blocked with 1% BSA and 10% horse serum. Cells were further incubated with Alexa-Fluor 488-labeled phalloidin, cortactin antibody and DAPI. Cells were viewed using an Olympus FV1000 Laser Scanning Confocal Microscope. Lamellipodia, the flattened F-actin-rich leading edge of migrating cells, were outlined and measured in length using the Image-Pro Plus software (Media Cybernetics, Rockville, MD, USA). The summed length of the lamellipodia was expressed as a percentage of total cell circumferences. The images are representative of at least 50 cells.

Determination of Mitochondrial Membrane Potential: The mitochondrial membrane potential was measured using the fluorescent dye TMRM.[51] Briefly, MDA-MB-231 cells were seeded into six-well cell culture plates, incubated with or without 50 μM AuNRs for 24 h and stained with 20 nM TMRM for 20 min at 37 °C. Next, cells were further harvested by trypsinization, washed with PBS and analyzed using a FACSCalibur flow cytometer and Cell Quest software (BD Biosciences).

Detection of Intracellular ATP Level: The intracellular ATP level was quantified using an ATP Assay Kit (Beyotime, Haimen, China). Briefly, MDA-MB-231 cells were seeded in six-well cell culture plates, incubated with the indicated AuNRs or compounds, lysed with 400 μl ice-cold ATP-releasing buffer for each well and centrifuged at 12 000 ×*g* for 10 min. After centrifugation, the supernatant was transferred into a new tube to test for ATP. The luminescence from a 10-μL sample was assayed in a Berthold Sirius single-tube luminometer (Berthold Technologies, Bad Wildbad, Germany) together with 100 μL of ATP detection buffer. The standard curve of ATP concentration was prepared from a known amount of ATP. ATP levels were then normalized according to the protein concentration.

Mitochondrial OXPHOS and Glycolysis Assays: Mitochondrial OXPHOS and glycolysis were analyzed using a Seahorse XF24 Extracellular Flux Analyzer (Seahorse Bioscience, North Billerica, MA, USA) by measuring the oxygen consumption rate (OCR, indicative of mitochondrial OXPHOS) and extracellular acidification rate (ECAR, indicative of glycolysis) in real time. For OCR analysis, cells were seeded in 24-well plates designed for XF24 at 20 000 cells per well in complete growth media. On the next day, the cells were treated with 50 μM AuNRs for 24 h, then switched to unbuffered media and further incubated in a CO_2-free incubator for 1 h prior to measurement. A program with typical 8-min cycle of mix (3 min), dwell (2 min) and measure (3 min) was set. During measurement, oligomycin, FCCP, antimycin A and rotenone were added at a final concentration of 1 μM (but 0.5 μM FCCP for PC3 cells). For ECAR analysis, cells were switched to a basal glucose-free medium before incubation in a CO_2-free incubator after AuNRs treatment. A default standard glycolysis stress test program was selected. In addition, the added compounds during measurement were glucose (final concentration 10 mM), oligomycin (final concentration 1 μM) and 2-deoxyglucose (final concentration 100 mM). At the end of each assay, protein quantification was performed for normalization.

Intracellular Trafficking and Localization of AuNRs by TEM: MDA-MB-231 cells were cultured on 60-mm petri dishes for 24 h and treated with 50 μM AuNRs for the following 3, 6 or 24 h. Three dishes of cells were used at each time point. Cells in each dish were washed with PBS three times, digested with 0.25% trypsin, centrifuged for 5 min at 1000 × *g* and subsequently collected. The cell pellets were fixed overnight in a fixation solution containing 2.5% glutaraldehyde in 0.1 M PBS. The pellets were then post-fixed with 1% OsO_4 in PBS for 1 h, dehydrated in a graded series of ethanol, treated with propylene oxide and embedded in Epon. Approximately 60 nm thick sections were cut, placed on carbon film supported by copper grids, stained with uranyl acetate and lead citrate and observed using Tecnai Spirit TEM at 100 kV.

Quantitative Proteomic Analysis: Cell culture for stable isotope labeling was performed as previously described. The heavy-labeled cells were incubated with 50 μM AuNRs at 37 °C for 24 h, while the light-labeled cells were left untreated as the control. Cells of each sample were washed with cold PBS, scraped into 8 M urea solution with protease inhibitor cocktail tablet and sonicated for lysis, separately. After centrifugation for 30 min at 20 000 ×*g*, the supernatants were collected and the protein concentrations were measured. Extracted protein samples from heavy-labeled cells and light-labeled cells were combined at a 1:1 ratio. In-solution digestion was performed with a sequence grade trypsin (Promega, Madison, WI, USA) at a ratio of 1:50 at 37 °C overnight. Digests were centrifuged at 13 000 ×*g* for 10 min and the supernatants were analyzed using two-dimensional liquid chromatography (2D-LC) on a LTQ Orbitrap XL (Thermo Fisher Scientific, Waltham, MA, USA).[52,53] Nanoelectrospray ionization was achieved with a spray voltage of 2.5 kV and a heated capillary temperature of 230 °C. A cycle of one full-scan mass spectrum (400–2,000 m/z) followed by six data-dependent tandem mass spectra was repeated continuously throughout each step of multidimensional separation. All tandem mass spectra were collected using a normalized collision energy of 35%, an isolation window of 3 m/z and one microscan. MS spectra (.raw) from the XCalibur data system (Thermo Fisher Scientific, Waltham, MA, USA) were processed using the MaxQuant software, and the derived peak lists were searched using the Mascot search engine (Matrix Science, London, U.K.) against a concatenated forward-reverse database from the National Center for Biotechnology information nonredundant (NCBinr) database containing human sequences. The search parameters allowed the inclusion of up to two missed cleavages. The initial mass deviation of precursor ions and fragment ions were up to 10 ppm and 0.5 Da, respectively. The posterior error probability (PEP) for peptide identification (MS/MS spectra) was below or equal to 0.1. The false positive rate (FPR) was set to 5% at the peptide level. Mascot search results were further processed using the MaxQuant program with the FPR 1% at the protein level. The normalized *H/L* ratio, significance and variability (%) were automatically produced by the MaxQuant program, included in a proteingroups.txt output file. Further bioinformatic analysis was performed based on Gene Ontology and KEGG database.

Real-Time Quantitative PCR Assays: MDA-MB-231 cells were treated with 50 μM AuNRs for 24 h or left untreated as the control. Total RNA was isolated using the RNeasy Plus Mini Kit (Qiagen, Shanghai, China) according to the manufacturer's protocols. Next, 1 μg RNA of each sample was used for cDNA synthesis using the RT^2 First Strand Kit (Qiagen). Quantification of mRNA for genes involved in glucose metabolism was performed using the RT^2 Profiler Human Glucose Metabolism PCR Arrays (Qiagen) based on SYBR Green technology according to the manufacturer's instructions. Real-time PCR was performed using an ABI 7300 Real-time PCR system (Applied Biosystems, Foster, CA, USA). Data analysis was completed using the RT^2 Profiler PCR Array Data Analysis Template v4.0 (Qiagen).

Tumor Growth and Metastatic Lung Assays: The mice used in this study were bred and maintained in a specific pathogen-free environment, and all experiments with mice were done following the guidelines for experimental animals and were approved by the Institutional Animal Care and Use Committee of Institute of Biophysics, Chinese Academy of Sciences (IACUC-IBP). For xenograft assays, MDA-MB-231 cells were injected subcutaneously into the flank of 6–8 weeks Balb/c nude mice (1.8×10^6 MDA-MB-231 control cells or 1.8×10^6 AuNRs-pretreated MDA-MB-231 cells, respectively) in 100 μL of PBS. In addition, the grown tumors were measured for their size after six weeks. For experimental metastasis assays, MDA-MB-231 cells were injected into the tail vein of 6–8 weeks Balb/c nude mice (5×10^6 MDA-MB-231 control cells or 5×10^6 AuNRs-pretreated MDA-MB-231 cells, respectively) in 200 μL of PBS. After 12 weeks, the mice were sacrificed, and the lungs were dissected, rinsed in PBS and fixed in 10% neutral-buffered formalin solution. Surface metastatic nodules of lungs were macroscopically

quantified. Furthermore, the lungs were paraffin-embedded, sectioned (5 μm thickness), stained with hematoxylin and eosin, scanned with a Leica SCN 400 scanner (Leica Microsystems Incorporation, Buffalo Grove, IL, USA), and the sectioned metastatic nodules were quantified.

Statistical Analysis: All data were expressed as the mean ± SEM unless otherwise indicated. Statistical significance was determined using two-sided Student *t* test unless otherwise indicated. $*P < 0.05$ was considered to be statistically significant.

Supporting Information

Supporting Information is available from the Wiley Online Library or from the author.

Acknowledgements

T.Z., M.Y., B.Z. contributed equally to this work. The authors thank Profs. Myron L. Toews (University of Nebraska Medical Center), Fuyu Yang and Fuquan Yang (Institute of Biophysics, Chinese Academy of Sciences) for critical reading and editing of the manuscript. The authors are indebted to Peng Xue and Yanxia Jia (Institute of Biophysics, Chinese Academy of Sciences) for technical assistance. This work was supported by grants from the National Basic Research Program of China (Grants 2012CB934003, 2010CB833701 and 2010CB933401), the National Natural Science Foundation of China (Grants 31100595 and 31300683), the Major Equipment Program of China (Grant 2011YQ030134), and the Nebraska State LB595 Research Program of USA.

Received: May 20, 2014
Revised: July 10, 2014
Published online: September 5, 2014

[1] D. Hanahan, R. A. Weinberg, *Cell* **2011**, *144*, 646.
[2] R. Siegel, D. Naishadham, A. Jemal, *Cancer J. Clin.* **2013**, *63*, 11.
[3] I. J. Fidler, *Semin. Cancer Biol.* **2002**, *12*, 89.
[4] A. C. Chiang, J. Massague, *N. Engl. J. Med.* **2008**, *359*, 2814.
[5] J. E. Talmadge, I. J. Fidler, *Cancer Res.* **2010**, *70*, 5649.
[6] C. L. Chaffer, R. A. Weinberg, *Science* **2011**, *331*, 1559.
[7] H. Yamaguchi, J. Condeelis, *Biochim. Biophys. Acta* **2007**, *1773*, 642.
[8] T. D. Pollard, G. G. Borisy, *Cell* **2003**, *112*, 453.
[9] D. R. Kovar, E. S. Harris, R. Mahaffy, H. N. Higgs, T. D. Pollard, *Cell* **2006**, *124*, 423.
[10] C. Le Clainche, M. F. Carlier, *Physiol. Rev.* **2008**, *88*, 489.
[11] J. H. Park, G. von Maltzahn, M. J. Xu, V. Fogal, V. R. Kotamraju, E. Ruoslahti, S. N. Bhatia, M. J. Sailor, *Proc. Natl. Acad. Sci. U.S.A.* **2010**, *107*, 981.
[12] S. K. Sahoo, S. Parveen, J. J. Panda, *Nanomedicine* **2007**, *3*, 20.
[13] F. Alexis, E. M. Pridgen, R. Langer, O. C. Farokhzad, *Handb. Exp. Pharmacol.* **2010**, *197*, 55.
[14] D. Farrell, J. Alper, K. Ptak, N. J. Panaro, P. Grodzinski, A. D. Barker, *ACS Nano* **2010**, *4*, 589.
[15] M. Tiwari, *J. Cancer Res. Ther.* **2012**, *8*, 19.
[16] V. M. Peterson, C. M. Castro, H. Lee, R. Weissleder, *ACS Nano* **2012**, *6*, 3506.
[17] K. H. Bae, H. J. Chung, T. G. Park, *Mol. Cells* **2011**, *31*, 295.
[18] L. Zhang, F. X. Gu, J. M. Chan, A. Z. Wang, R. S. Langer, O. C. Farokhzad, *Clin. Pharmacol. Ther.* **2008**, *83*, 761.
[19] L. Vigderman, B. P. Khanal, E. R. Zubarev, *Adv. Mater.* **2012**, *24*, 4811.
[20] D. Pissuwan, S. M. Valenzuela, M. B. Cortie, *Biotechnol. Genet. Eng. Rev.* **2008**, *25*, 93.
[21] C. M. Cobley, J. Chen, E. C. Cho, L. V. Wang, Y. Xia, *Chem. Soc. Rev.* **2011**, *40*, 44.
[22] A. M. Alkilany, L. B. Thompson, S. P. Boulos, P. N. Sisco, C. J. Murphy, *Adv. Drug Delivery Rev.* **2012**, *64*, 190.
[23] J. V. Jokerst, A. J. Cole, D. Van de Sompel, S. S. Gambhir, *ACS Nano* **2012**, *6*, 10366.
[24] L. Wang, X. Lin, J. Wang, Z. Hu, Y. Ji, S. Hou, Y. Zhao, X. Wu, C. Chen, *Adv. Funct. Mater.* **2014**, *24*, 4229.
[25] A. Albanese, P. S. Tang, W. C. W. Chan, *Annu. Rev. Biomed. Eng.* **2012**, *14*, 1.
[26] Y. Qiu, Y. Liu, L. M. Wang, L. G. Xu, R. Bai, Y. L. Ji, X. C. Wu, Y. L. Zhao, Y. F. Li, C. Y. Chen, *Biomaterials* **2010**, *31*, 7606.
[27] L. G. Xu, Y. Liu, Z. Y. Chen, W. Li, Y. Liu, L. M. Wang, Y. Liu, X. C. Wu, Y. L. Ji, Y. L. Zhao, L. Y. Ma, Y. M. Shao, C. Y. Chen, *Nano Lett.* **2012**, *12*, 2003.
[28] W. Zhang, Y. Ji, X. Wu, H. Xu, *ACS Appl. Mater. Interfaces* **2013**, *5*, 9856.
[29] C. Grabinski, N. Schaeublin, A. Wijaya, H. D'Couto, S. H. Baxamusa, K. Hamad-Schifferli, S. M. Hussain, *ACS Nano* **2011**, *5*, 2870.
[30] L. M. Wang, Y. Liu, W. Li, X. M. Jiang, Y. L. Ji, X. C. Wu, L. G. Xu, Y. Qiu, K. Zhao, T. T. Wei, Y. F. Li, Y. L. Zhao, C. Y. Chen, *Nano Lett.* **2011**, *11*, 772.
[31] L. M. Zhang, L. M. Wang, Y. L. Hu, Z. G. Liu, Y. Tian, X. C. Wu, Y. L. Zhao, H. R. Tang, C. Y. Chen, Y. L. Wang, *Biomaterials* **2013**, *34*, 7117.
[32] X. H. Huang, S. Neretina, M. A. El-Sayed, *Adv. Mater.* **2009**, *21*, 4880.
[33] M. P. Monopoli, C. Aberg, A. Salvati, K. A. Dawson, *Nat. Nanotechnol.* **2012**, *7*, 779.
[34] S. Tenzer, D. Docter, J. Kuharev, A. Musyanovych, V. Fetz, R. Hecht, F. Schlenk, D. Fischer, K. Kiouptsi, C. Reinhardt, K. Landfester, H. Schild, M. Maskos, S. K. Knauer, R. H. Stauber, *Nat. Nanotechnol.* **2013**, *8*, 772.
[35] C. D. Walkey, J. B. Olsen, F. Song, R. Liu, H. Guo, D. W. H. Olsen, Y. Cohen, A. Emili, W. C. W. Chan, *ACS Nano* **2014**, *8*, 2439.
[36] L. M. Wang, J. Y. Li, J. Pan, X. M. Jiang, Y. L. Ji, Y. F. Li, Y. Qu, Y. L. Zhao, X. C. Wu, C. Y. Chen, *J. Am. Chem. Soc.* **2013**, *135*, 17359.
[37] R. R. Arvizo, S. Saha, E. Wang, J. D. Robertson, R. Bhattacharya, P. Mukherjee, *Proc. Natl. Acad. Sci. U.S.A.* **2013**, *110*, 6700.
[38] Y. Xie, D. W. Wolff, T. Wei, B. Wang, C. Deng, J. K. Kirui, H. Jiang, J. Qin, P. W. Abel, Y. Tu, *Cancer Res.* **2009**, *69*, 5743.
[39] L. I. Cosen-Binker, A. Kapus, *Physiology (Bethesda)* **2006**, *21*, 352.
[40] A. G. Ammer, S. A. Weed, *Cell Motil. Cytoskeleton* **2008**, *65*, 687.
[41] M. F. Carlier, D. Pantaloni, *J. Biol. Chem.* **2007**, *282*, 23005.
[42] G. J. Doherty, H. T. McMahon, *Annu. Rev. Biochem.* **2009**, *78*, 857.
[43] G. Sahay, D. Y. Alakhova, A. V. Kabanov, *J. Controlled Release* **2010**, *145*, 182.
[44] T. B. Huff, M. N. Hansen, Y. Zhao, J. X. Cheng, A. Wei, *Langmuir* **2007**, *23*, 1596.
[45] T. S. Hauck, A. A. Ghazani, W. C. Chan, *Small* **2008**, *4*, 153.
[46] N. Mizushima, T. Yoshimori, B. Levine, *Cell* **2010**, *140*, 313.
[47] M. Ashburner, C. A. Ball, J. A. Blake, D. Botstein, H. Butler, J. M. Cherry, A. P. Davis, K. Dolinski, S. S. Dwight, J. T. Eppig, M. A. Harris, D. P. Hill, L. Issel-Tarver, A. Kasarskis, S. Lewis, J. C. Matese, J. E. Richardson, M. Ringwald, G. M. Rubin, G. Sherlock, *Nat. Genet.* **2000**, *25*, 25.
[48] T. Schlitt, K. Palin, J. Rung, S. Dietmann, M. Lappe, E. Ukkonen, A. Brama, *Genome Res.* **2003**, *13*, 2568.
[49] M. Yi, J. D. Horton, J. C. Cohen, H. H. Hobbs, R. M. Stephens, *BMC Bioinf.* **2006**, *7*, 30.
[50] A. Boire, L. Covic, A. Agarwal, S. Jacques, S. Sherifl, A. Kuliopulos, *Cell* **2005**, *120*, 303.
[51] H. Zhou, B. Zhang, J. Zheng, M. Yu, T. Zhou, K. Zhao, Y. Jia, X. Gao, C. Chen, T. Wei, *Biomaterials* **2014**, *35*, 1597.
[52] H. C. Harsha, H. Molina, A. Pandey, *Nat. Protoc.* **2008**, *3*, 505.
[53] C. Delahunty, J. R. Yates, *Methods* **2005**, *35*, 248.